THESIS

CORRELATED ELECTRON MICROSCOPY WITH ELECTRO-OPTICAL IMAGING OF HEXAGONAL TUNGSTEN OXIDE NANORODS

Submitted by

Christina J. Cashen

Department of Chemistry

In partial fulfillment of the requirements

For the Degree of Master of Science

Colorado State University

Fort Collins, Colorado

Summer 2019

Master's Committee

Advisor: Justin B. Sambur

Amy Prieto
Yan Vivian Li

ABSTRACT

CORRELATED ELECTRON MICROSCOPY WITH ELECTRO-OPTICAL IMAGING OF HEXAGONAL TUNGSTEN OXIDE NANORODS

Fundamental understanding of the dynamics of ion insertion into a host material are essential to accommodate the rising demand for energy storage technology. It has been established that single nanoparticle electrodes greatly improve the kinetics of the ion insertion reaction, however the heterogeneous behavior of single particles correlated to the structure of the particle has been challenging to determine. This work takes on this challenge by developing a method that implements optical microscopy to study the optical modulations of electrochromic single particle hexagonal tungsten oxide (*h*-WO_3) nanorods with transmission electron microscopy (TEM). Heightened resolution provided by TEM reveals sub-atomic structural details which would be impossible to observe with other techniques. This work introduces a method of measuring correlated single particle optical activity of WO_3 with TEM resolution images of the same particle. This study found heterogeneous optical modulations of the carbon film considerably influenced the optical activity of WO_3. Bearing in mind this behavior is vital for future experiments using this method. After this is accounted, we compare the optical activity of two single particles using the common parameters: maximum optical density (max OD) and the time it takes to reach 90% of the max OD (t_{90}). This comparison provides further evidence that the presence of nanosized step-edge gradients contribute to the ion insertion dynamics of this electrochromic host material.[1] Further study using this method can reveal a understanding of how the presence of step-edges contributes to the local lattice dynamics upon lithiation of a nanorod.

ACKNOWLEDGMENTS

There are many people who made accomplishing this achievement possible. This work would not have come to fruition without the intellectual and technical input from Colby Evans, Justin Sambur, Michael Van Erdewyk, Zach Nilsson, Lacey Beck, and Max Schulze. Special thanks towards Zach Nilsson for spending hours listening to my instructions whilst operating and acquiring hundreds of TEM images. I would like to thank Fionna Samuels, Chris Rom, Michael Van Erdewyk, Sam Miller and Colby Evans for the time they spent reading my manuscripts and offering editorial comments. Thank you to Mom and Dad, I would not be where I am without you. Thank you to my Bart family (Nicki, Tony, Brooke, Anthony, Cash, Grandpa Tony and Tammy) for creating a family community for me in Colorado and showing me a new meaning of family support. I have the utmost gratitude to Nicole Bondy, for her unwavering support, constant listening ear, compassionate spirit, and grounding presence. Lastly, I'd like to thank the generations of female scientists that came before me, that opened the doors for me in a laboratory setting. It is thanks to you that I have a seat at this table and the opportunity to do this work. Onward.

TABLE OF CONTENTS

ABSTRACT ii
ACKNOWLEDGMENTS iii
Introduction 1
Methods 6
    Synthesis of Material 6
    Electrochemical Cell Design 7
    Opto-electrochemical Measurements 8
    Image Processing and Analysis 9
Results and Discussion 13
    Carbon Film Optical Activity 13
    Single Particle Correlated Electro-optical TEM Analysis 19
Conclusions 22
Outlook 23
References 25

Introduction

Energy storage technology such as Li-ion batteries and electrochromic smart windows[2–5] rely on ion insertion/extraction processes. One strategy to improve the efficiency, rate, and reversibility of ion insertion/extraction process is to employ nanostructured electrode materials. Electrode materials with nanometer dimensions reduce ion and electron transport lengths and therefore improve ion insertion/extraction kinetics [6–11]. However, nanoscale materials are structurally heterogenous in that the size, shape, and morphology vary from particle to particle. Understanding how particle-to-particle structural heterogeneity contributes to underlying ion insertion/extraction efficiency and kinetics is critical to improving electrochemical energy storage technologies[12,13].

Individual nanoparticles exhibit intrinsic composition and structural heterogeneity, necessitating the study of nanoparticle electrodes at the single particle level.[14,15] Ideally, single particle-level studies would capture electrochemical kinetics at the single particle-level and correlate that information with atomic-level structure in real time. Towards this goal, several groups have developed *in-operando* electron[16–18], X-ray[15,19], electrochemical, Raman[7,20,21] and optical microscopy approaches[8,16,22] to study ion insertion and extraction processes at the single particle-level. Electron and X-ray microscopy methods have the potential to correlated single particle electrochemistry with atomic-level or nanometer spatial resolution. Huang and co-workers first developed an electrochemical cell that could be operated in a transmission electron microscope (TEM) for correlated electrochemical and TEM measurements of Li-ion insertion in single SnO_2 nanowire anodes[23]. The authors correlated the electrochemical lithiation kinetics with detailed structural evolution at the nanowire surface and in the bulk. This *in-operando* TEM approach has been extended to study ion insertion process in nanoscale materials[24–26]. Specifically,

Bai *et al* extended this methodology to study Li-ion insertion in single monoclinic-WO_3 nanowire[8,27,28]. The authors collected TEM images over time of the lithiation of a nanowire at the single particle level and correlated those dynamics with a lithiation front that progresses through the nanorod over time, however the neither of these studies report correlated electrochemical measurements to the nanorod observed.

Tada and co-authors designed an experiment to acquire *in-situ* time-resolved X-ray absorption fine structure spectra (XAFS) of single Pt complex catalyst anode particles with nanometer resolution. This study was able to reveal the rate constants of the dynamic surface event upon electrochemical cycling of the material.[15] While *in-operando* TEM and X-ray measurements are extremely powerful tools that provide atomic-level structural and composition information, those measurements typically require specialized instrumentation and/or synchrotron light sources. Since the electrochemical response stems from many nanoparticles on the electrode, *in-operando* TEM measurements do not often link single particle-level electrochemical data with high resolution structural information. Moreover, the extent to which the high energy electron and X-ray radiation doses impact the underlying electrochemical processes remains unclear.

An alternative approach to link electrochemical kinetics with high resolution structural information is to perform electrochemical measurements at the single particle-level and then perform ex situ SEM or TEM measurements on the same particles in a one-to-one fashion. A recent scanning electrochemical cell microscopy (SECCM) study by Unwin and co-workers measured the lithiation kinetics of single $LiMn_2O_4$ battery particles[29,30]. The authors correlated the electrochemical response of 12 particles with the particle morphology as determined by ex situ SEM. It is notable that SECCM is compatible with ex situ TEM, but this has not been applied to Li-ion insertion electrochemistry. While the SECCM approach can be applied in a high-throughput

manner the point-by-point approach does not capture electrochemical data on a large number of nanoparticles at the same time.

We have recently developed an alternative widefield electro-optic imaging approach to measure electrochemical data at the single particle-level. In this approach, we use optical microscopy analysis of an electrochromic host material at the single particle level, coupled with *ex-situ* TEM measurements to gain sub-atomic structural resolution of the correlated nanoparticle, allowing us to overcome previous spatial and structural resolution issues in other works.

Electrochromic materials have the unique feature of changing color upon an applied electric field. The most widely studied electrochromic material, tungsten oxide (WO_3), is a white powder in its pristine form. [31–35] Depositing this material onto a transparent, electrically conductive substrate coupled with an ion source, and applying a cathodic potential causes W^{6+} to reduce to W^{5+} as an ion is injected into the material (M_xWO_3), resulting in a blue tint. This reaction is represented by Equation 1, where M^+ is a cation able to insert into the crystal (H^+, Li^+, K^+, Mg^{2+}, Al^{3+}, etc.).[20,34,36,37] Conversely, applying an anodic potential extracts electrons and ions and the material returns to its original transparent state.

$$xM^+ + xe^- + WO_3 \leftrightarrow M_xWO_3 \qquad (1)$$

When the material is in a tinted state, the absorption of infrared radiation dramatically rises, blocking thermal radiation that would otherwise pass through the transparent substrate. [38,39] Because the ion insertion reaction into WO_3 results in an optical reaction, we measure this reaction using optical microscopy. Optical microscopy exhibits several features that are suitable for *in-situ* imaging the electrochemical reactions of single nanoparticles, including high temporal resolution, noninvasiveness, high throughput, and low cost.[40–43] In this work we use correlated single particle-level optical imaging coupled with *ex-situ* TEM images to better quantify the role of structural

features that may contribute to the structure-activity relationship of a hexagonal tungsten oxide (*h*-WO_3) particle. This study focuses solely on *h*-WO_3 due to previously identified Li^+ intercalation sites. Three possible Li^+ binding sites are present in this structure: trigonal cavities (TC), hexagonal windows (HW) and square windows (SW), pictured in Figure 1.[1]

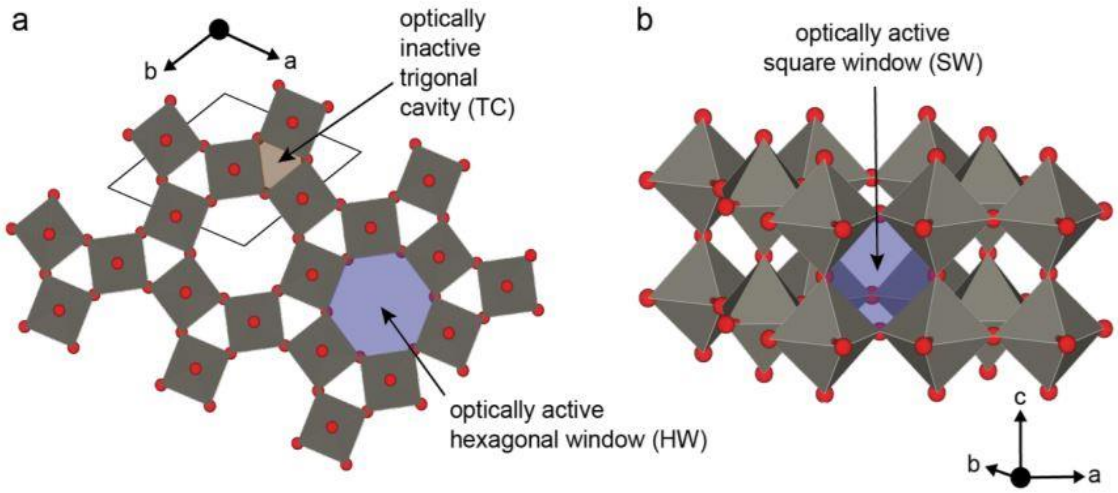

Figure 1.Illustration of the *h*-WO_3 crystal structure with the three possible binding sites for ions, and the corresponding optical behavior of those sites.

Previous studies have found that ions bind to these sites at different rates and illicit different optical responses. The optical behavior of *h*-WO_3 on the transparent electrically conductive substrate tin doped indium oxide (ITO) has previously been studied and modeled to understand ion insertion kinetics of Li^+ into the material.[1] Hibino *et al* found that trigonal cavities are the most stable sites for Li^+ ions, followed by hexagonal windows and square windows.[44] Followed by Balaji *et al* determining that lithium that is bound in the trigonal cavities, does not lead to optical activity, while hexagonal and square windows do.[20]

This study aims to understand how finite structural characteristics of a single particle can lead to differences in optical behavior. Due to heterogeneous surface structure features, exposure of these binding sites to Li^+ ions can differ from particle to particle. To better quantify these

features, this work performs electrochemical experiments of *h*-WO_3 on a TEM grid substrate, rather than ITO, to enable *ex-situ* TEM measurements of single particles. This reveals minute morphological and structural features of WO_3 particles that supports the model presented in previous work.[1] The results of changing the substrate from ITO to TEM grid reveals optical behavior of the substrate itself that has not yet been reported[17,45], demonstrating that determining background incident light is a major challenge. Taking this phenomenon into account is vital in the analysis of single particle optical behavior within this system. We find that the relationship between finite structural resolution and optical activity of a single nanoparticle supports the claims made in previous work, while introducing a new methodology to expand the resolution of a well-studied system.

Methods

Synthesis of Material

h-WO_3 nanorods were synthesized and stabilized via the methodology described by Wang *et al*.[11] Following the synthesis pathway:

$$Na_2WO_4 + 2HCl \rightarrow H_2WO_4 + 2NaCl$$

$$H_2WO_4 \rightarrow WO_3 + H_2O$$

Precursors include 0.5798 g of NaCl (Fisher Scientific) and 0.8250 g of $Na_2WO_4 \cdot 2H_2O$ (Mallinckrodt Chemical Works) which were dissolved into 19 mL of 18.2 MΩ filtered H_2O. While stirring, 850 µL of 3 M HCl was slowly added to achieve a solution with pH 2.06. The pH was monitored by using a pH meter (HACH HQ11d). This solution was then placed into a Parr Acid Digest hydrothermal reactor and heated in a convection oven at 180 °C for 24 hours, then taken out of the oven and allowed to cool to room temperature on the benchtop. The supernatant was pipetted out and a white powder was recovered. The product was washed and stored in 18.2 MΩ filtered H_2O. The WO_3 hexagonal phase was confirmed (JCPDS 00-033-1387) via powder x-ray diffraction (PXRD) by using a Bruker D8 Discover Series II X-ray Diffractometer (PXRD), with Cu Kα ($\lambda = 0.15406$ nm) radiation at 50 kV and 50 mA in a 2θ range from 10° to 80° at room temperature on a zero-diffraction silicon wafer (MTI Chemical Corp.)

Electrochemical Cell Design

The electrochemical cell (Figure 2b & c) consists of WO_3 nanoparticles deposited, via spin coating, onto a Ni TEM Grid (Ted Pella PELCO® 200 Mesh Ni Grid). The TEM grid is sandwiched between two pieces of customized hardware: a 3D printed polyethylene terephthalate glycol (PETG) reservoir, and a Ni foil (Sigma-Aldrich,>99.9% Ni). This set up allows for transmission imaging of the particles through the TEM grid alone, while maintaining electrical contact to the Ni foil (working electrode) and contact with the electrolyte contained in the reservoir. During assembly, a voltmeter is used to check the TEM grid and Ni foil have electrical contact. The counter (CE) and reference (RE) electrodes are secured through two holes in the side of the reservoir (Figure 2b). All electrochemical measurements used Ag/AgCl as a reference electrode and Pt wire (Alfa Aesar, 99.95%), as a counter electrode. Once the TEM grid is sandwiched between coverslip, Ni foil, and the reservoir, the cell is mechanically secured using insulating epoxy (Loctite E-120HP Hysol). When the epoxy has cured a solution of 1 M lithium perchlorate ($LiClO_4$) in propylene carbonate (PC) is added into the reservoir. This solution is the lithium source and electrolyte used in all electrochemical experiments. When optical measurements are complete the TEM grid is mechanically removed from the cell, washed in dimethyl carbonate and then taken for *ex-situ* TEM measurements. TEM images were collected on a JOEL JEM1400 transmission electron microscope at a working voltage of 200keV.

Opto-electrochemical Measurements

Bright field transmission images are collected using an inverted microscope (Olympus

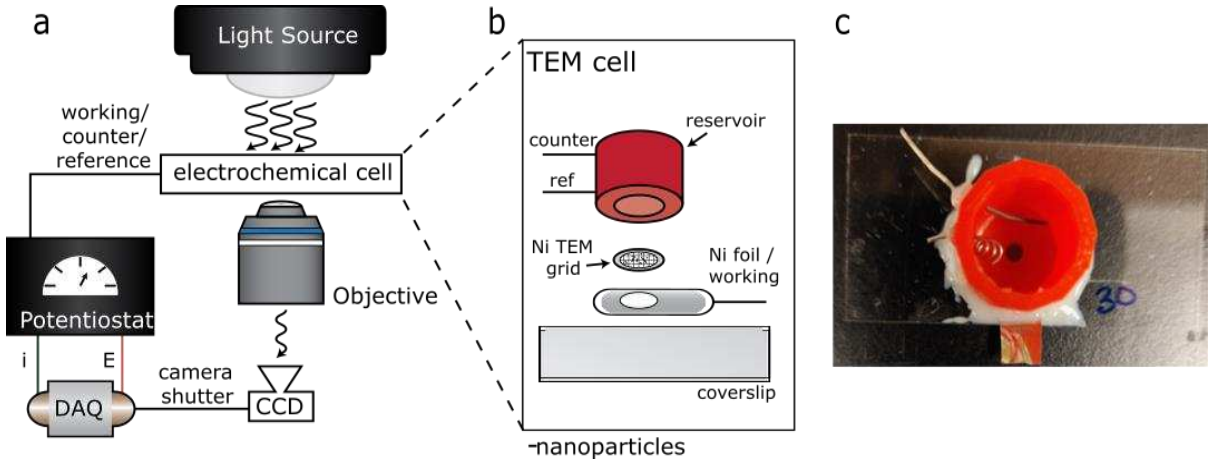

Figure 2. a) Inverted bright field opto-electrochemical measurement setup. b) Illustration of electrochemical TEM cell assembly. C) Picture of a finished electrochemical TEM cell post-assembly.

IX73) and a 100× objective (UPLANSAPO100x/W) accompanied with a 2× magnification lens to achieve 200× magnification and an Andor (iXON) EMCCD detector (Figure 2a). To simulate infrared radiation a 940 nm light emitting diode (LED) (Thor Labs) was the light source. Electrochemical measurements were conducted using an Autolab potentiostat (PGSTAT128N) *in-operando* with optical imaging. Chronoamperometry was the electrochemical method implemented to apply 3 cathodic and 3 anodic potential pulses for 30 seconds each. Coloration (cathodic pulse) and bleaching (anodic pulse) of the material occurred at potentials -1.0 V and +0.5 V vs Ag/AgCl, respectively. Electrochemical signals, potential and current, and camera shutter signals are acquired simultaneously via a data acquisition card (DAQ) to precisely synchronize the signals to the same time scale measurements. This method of optical imaging results in image stacks or "movies" that are analyzed to measure changes in pixel intensity within the image over time. All data collected was further organized and processed using a home-written MATLAB program.[1]

Image Processing and Analysis

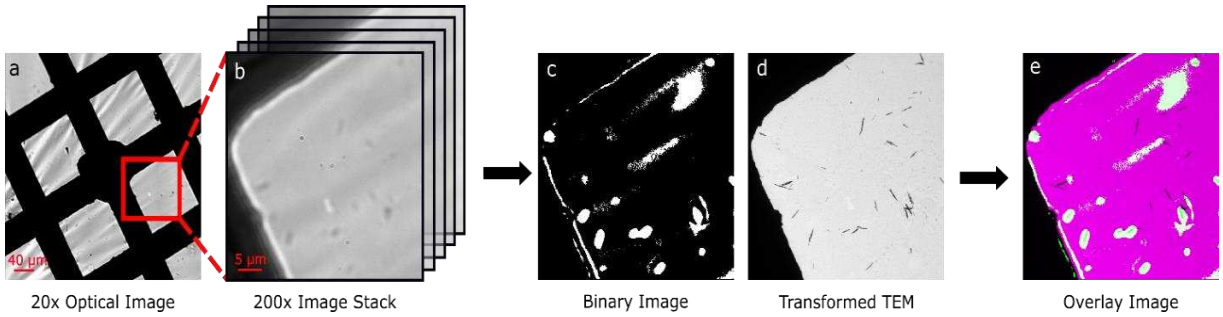

Figure 3. a) Bright field transmission optical micrograph (20x) of the center of the TEM grid within the electrochemical cell, with the area analyzed (ROI) outlined in red. b) Optical micrograph (200x) of the area of interest in which a movie was taken. c)Processed binary image. d) Transformed TEM image. e) Overlay of images c) and d).

Figure 3a shows a representative 20× bright field image of WO_3 nanoparticles deposited onto a Ni TEM grid working electrode. The TEM grid is composed of Ni bar supports with an amorphous carbon coating deposited over the Ni bars. The amorphous carbon windows support the WO_3 particles, provide electrical contact to the Ni bars, and allow for both optical and electron microscopy. The Ni bars and *h*-WO_3 particles appear as dark contrast pixels in the image, both due to blocking the transmission of light to the camera. Figure 3b shows a 200× transmission image of the red square box region in Figure 3a. The dark one-dimensional-like objects are *h*-WO3 particles and the solid dark object to the left and upper area of the image is Ni bar in TEM grid. In a typical experiment we apply potentials via chronoamperometry and record transmission images over time to make a movie.

Once a movie is collected further image processing is implemented to reveal the locations of electroactive particles on the TEM grid. (Figure 3c) This process involves the use of home-written MATLAB code to collect all frames during a coloring potential pulse resulting in WO_3 particles undergoing lithiation. Averaging these collected frames produces an average color pulse image. The same averaging process is applied to all frames during an anodic potential pulse resulting in particles delithiating, or bleaching, to produce an average bleach pulse image. The

difference between the average color and bleach image is calculated to produce a new subtracted image. A histogram is used to sort the intensities of each pixel in this subtracted image and a Gaussian fit is applied to the histogram. Most pixels attribute to the background, as the difference between the background pixels will be relatively low. A threshold was set at two standard deviations, 2σ, of all pixels to determine which pixels had a significant difference value, indicating a significant optical change. Any pixels greater than 2σ are assigned as a 1, and any pixel value less then 2σ is assigned a 0. Figure 3c shows the resulting binary image where white pixels are 1 and black pixels are 0. The white pixels in the binary image represent any significant optical activity that occurs within a movie between a coloring and bleach pulse. However, the binary image does not reveal spatial resolution of all particles present in Figure 3b, suggesting that not all particles are optically active.

A separate image process is conducted to produce spatial resolution of all nanoparticles in Figure 3b with higher resolution. This begins with an *ex-situ* TEM image of the same area as an optical movie taken to assess spatial distribution of particles. Four to five coordinates of the same objects in the TEM image and the optical image are collected to compute a geometrical transformation matrix. The MATLAB function tform computes the transformation matrix to produce a transformed TEM image (Figure 3d) that possesses the known relative dimensions as the optical image. The produced image allows for spatial resolution of all particles in the movie that are otherwise difficult to resolve using the optical image alone. Once the processed images shown in Figure 3c & d are produced, the two images are superimposed over one another to produce Figure 3e allowing a map of spatially resolved object correlated optical activity within the movie to be identified. The overlay image spatially reveals which white pixels correspond to an optically active nanoparticle.

This overlay image is used to draw masks on any qualitatively active (white pixels) or inactive (black/pink pixels) object. We note that there are particles within the movie that are qualitatively active: the collection of white pixels on top of a black object, shown circled in solid blue (Figure 4a). The integrated pixel intensity of the area circled in solid blue is taken (I), followed by a dashed blue mask adjacent to the nanorod to account for background (I_o) to calculate optical density (OD) as a function of time, using equation 2.

$$OD(t) = -log_{10}\left(\frac{I(t)}{I_o(t)}\right) \qquad (2)$$

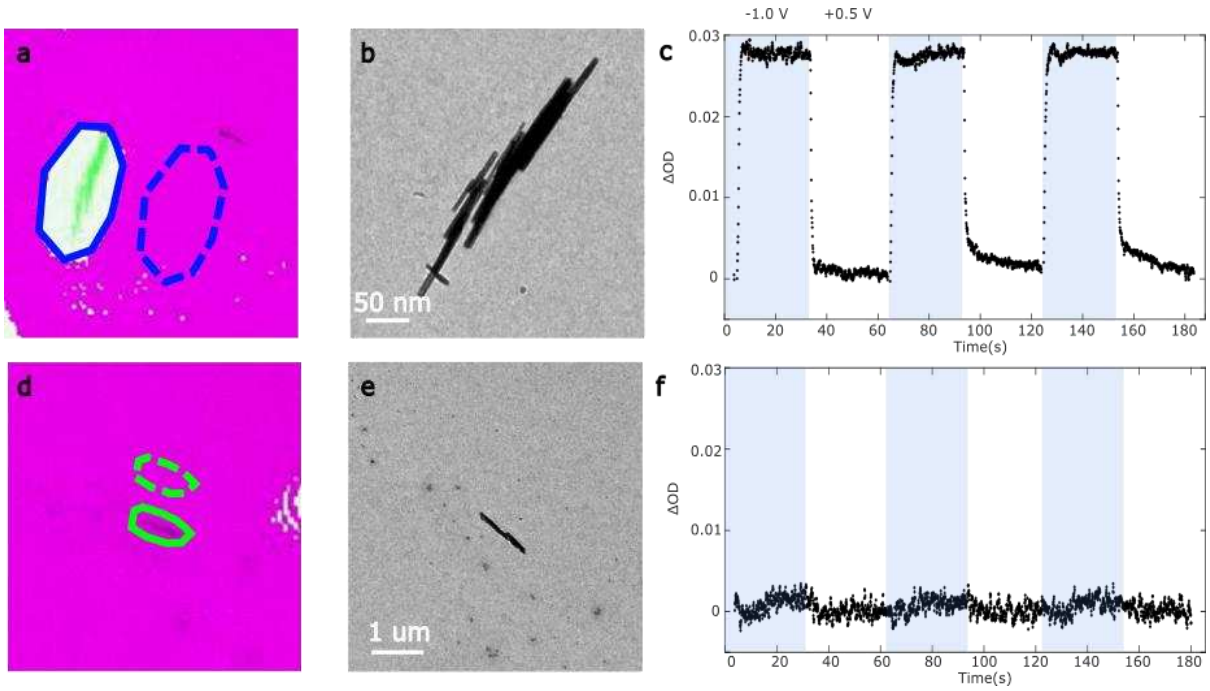

Figure 4. a) & d) Overlay image of TEM transformed and optical binary images. Particle mask (I) is outlined with solid blue or green and the background mask (I_o) is outlined with a dashed blue or green line. b) TEM image of a cluster of optically active nanoparticles outlined in blue. c) Optical trajectory produced from the cluster of nanoparticles shown in panel a). Blue shading indicates a coloring potential pulse, followed by a bleaching potential pulse. e) TEM image of a cluster of optically inactive nanoparticles outlined in green. f) Optical trajectory produced from the cluster of nanoparticles

Figure 4 is an example of the processed data that can be produced using the methods outlined in equation 2 and Figure 3. Figure 4a & d use the same overlay image presented in Figure 3e to locate a representative active and an inactive particle. A blue solid mask is drawn onto the object of interest (I) and a dashed blue line mask of the same dimensions is drawn next to the

object of interest (I_o). Figure 4b is a TEM image of the cluster of WO_3 nanoparticles within the blue circled mask, followed by the corresponding calculated OD trajectory (Figure 4c). The blue shading in Figure 4c indicates the time in which a coloring pulse of –1.0 V was applied to the cell, followed by a bleaching pulse of +0.5 V. When a coloring pulse is applied the OD(t) rises and plateaus, indicating that the particles are absorbing 940 nm light in this condition until a bleaching pulse is applied, resulting in OD(t) decreasing until particles reach their transparent/bleached state.

$$\Delta OD(t) = OD(t) - OD(0) \quad (3)$$

We calculate the change in OD (ΔOD) via equation 3, to determine the normalized OD change upon applied potentials. These results are representative of the optical behavior of this material under similar conditions based on previous studies.[1] The absence of white pixels on top of nanoparticle objects indicates that there are a significant number of qualitatively inactive particles (Figure 4d). Figure 4e & f shows a representative cluster of nanoparticles with the corresponding optical trajectory showing that this cluster does not exhibit significant optical changes upon any applied potential. With this analysis, we can analyze the optical behavior of any object within the ROI and produce TEM resolved images of that object.

Results and Discussion

Carbon Film Optical Activity

To establish the role the Ni TEM grid substrate plays in this system we examine the TEM grid using the optical microscope. Optical images of the Ni TEM grid reveal streak like features within the windows of the TEM grid (Figure 5 b & c) that are not present in a TEM image of the same area (Figure 5a). The light and dark streak features appear in the optical images due to

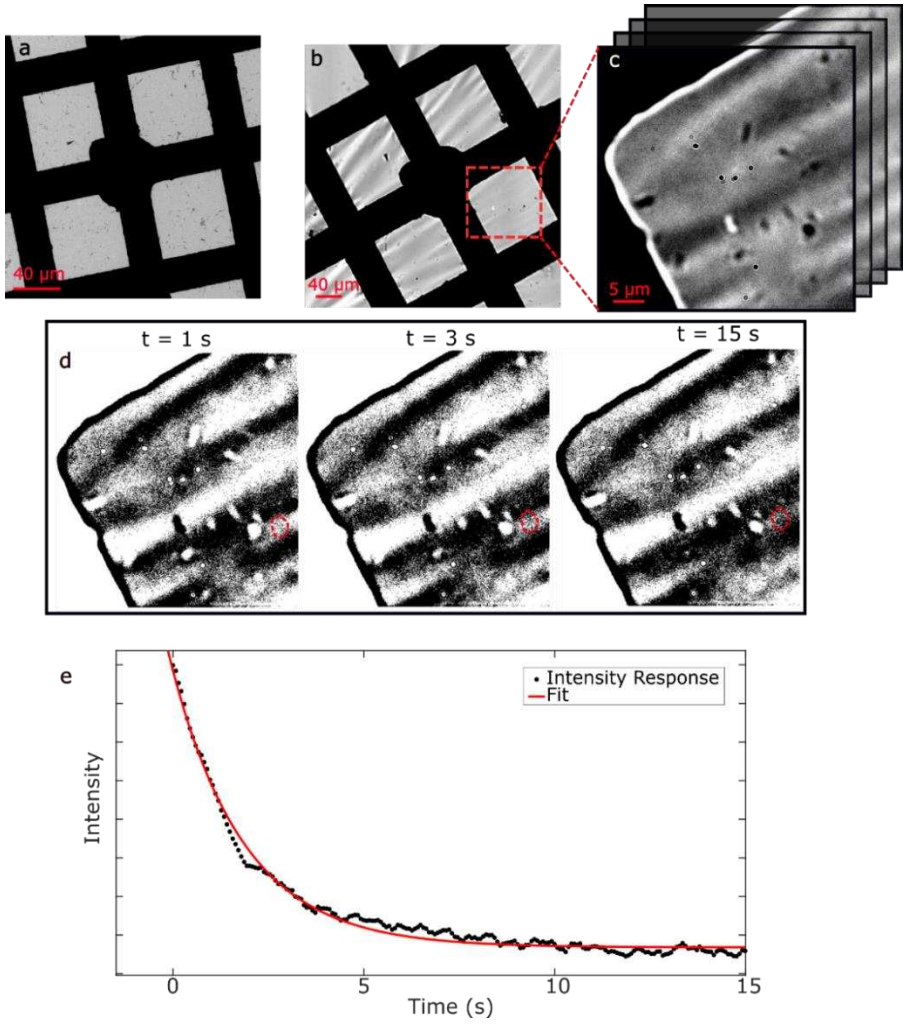

Figure 5. a) TEM image of WO_3 nanoparticle deposited onto a Ni TEM grid. b) Optical image taken at 20x magnification of the same area shown in panel a). c) An image stack or "movie" collected via optical microscopy at 200x magnification of a window outline with a red box in panel b). d) Three images taken from the image movie set to a threshold to create a binary that enhances the streaks present from the carbon film. The three images are taken one second, three seconds, and fifteen seconds after a potential step. e) Intensity trace (black dots) of the integrated pixel intensity of the area indicated by a red mask in d) throughout 15 seconds after a potential step occurred. The intensity trace is fit with an exponential decay shown in red.

changes in intensity manifested from folding of the carbon film on the TEM grid[46]. These streak features are enhanced by applying a threshold to the image in Figure 5c, to produce the binary images in Figure 5d. The three images in Figure 5d are images taken one, three, and fifteen seconds after a potential step occurred. We note that these streak features can optically and spatially change upon an applied potential step. To show an effect of the movement of these streaks, we drew a mask on the binary images, shown in red, of the dynamic folding feature. The intensity of these three separate images decreases over time, even though there are no particles present, indicating the intensity changes are a manifestation of the carbon film. To fully characterize the intensity changes, the mask is placed on all images in the span of the beginning of the potential step to 15 seconds after the potential step. The images are collected and the integrated intensity of the area within the mask is collected and shown in Figure 5e. This trace shows the decrease in intensity of the area of the carbon film outlined by the red mask over time. We note that this sharp change in intensity occurs upon any potential step. We recognize the behavior of this rate of decay to appear as an exponential decay, therefore, we fit the trace to an exponential decay shown in red in Figure 5e. Due to the goodness of fit of an exponential decay upon any applied potential, this suggests an association of double layer charging to the optical behavior observed.

To better understand this unexpected optical activity of the carbon film that would be considered the background or incident light, further analysis of the carbon film alone is performed and shown in Figure 6. Masks are drawn on 4 areas of the image that are representative of 4 types of observed background optical behaviors (Figure 6a). By using the overlay image as a guide, the masks are not drawn over any WO_3 particles. The 4 types of behavior are color coordinated such that Type 1 is blue, Type 2 is red, Type 3 is green, and Type 4 is cyan. The blue mask is drawn in the same location as the mask drawn in Figure 5d.

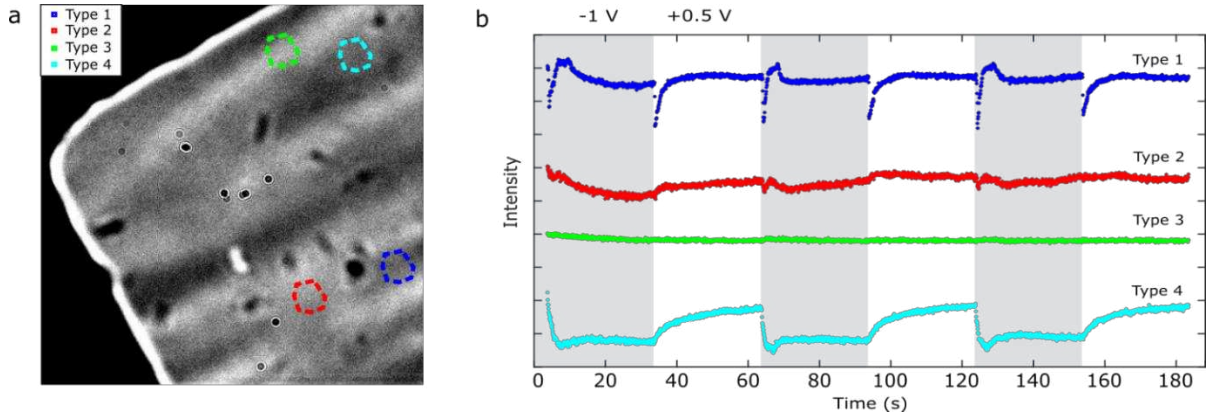

Figure 6. a) Optical image taken from the image stack shown in Figure 5. 4 types of background behaviors are spatially shown by 4 masks drawn onto the overly image. b) 4 trajectories corresponding to the 4 masks drawn in a) are shown

Intensity trajectories of the 4 masks drawn in Figure 6a are set to the same scale and displayed at an offset in Figure 6b. Type 1 is an observed spike in intensity upon any applied potential. We hypothesize that this optical response arises from strain on the film due to double later charging, thus the film folds upon itself or stretches itself producing a sudden darkening or lightening optical response. Once charging is complete, and the carbon film relaxes, the intensity returns to a stabilized value. Type 2 is an anomalous behavior resulting from the applied electrochemical stimuli. We hypothesize that this response is a result of the numerous cycles of charging. As the carbon film buckles and stretches over time, this mechanical stress results in a long-term deformation and strain of the film, producing irregular optical changes over time. Type 3 shows no associated optical reaction to applied electrochemical stimuli. This type of optical behavior is one typically associated with a background trajectory, as little to no optical changes occur throughout the movie. Type 4 displays behavior similar to the WO_3 nanoparticles themselves (Figure 6b), yet the trajectory pulled is of an area in which no WO_3 nanoparticles are present. This indicates that areas of the amorphous carbon are coloring as a coloring potential is applied. It has been shown previously that Li^+ ion transport is possible within the carbon film on a TEM grid,[17,45] yet this phenomena has not been optically measured previously. Furthermore, it has been observed

that the carbon film on a TEM grid exhibits spatial "summits" and "valleys" of the film[46]. When comparing that particle activity on the substrate ITO, ~6% of particles remained inactive, while 58% are inactive on a carbon film substrate.[1] This suggests that the activity of the carbon film substrate could be a reason for the lack of optical activity of the particles.

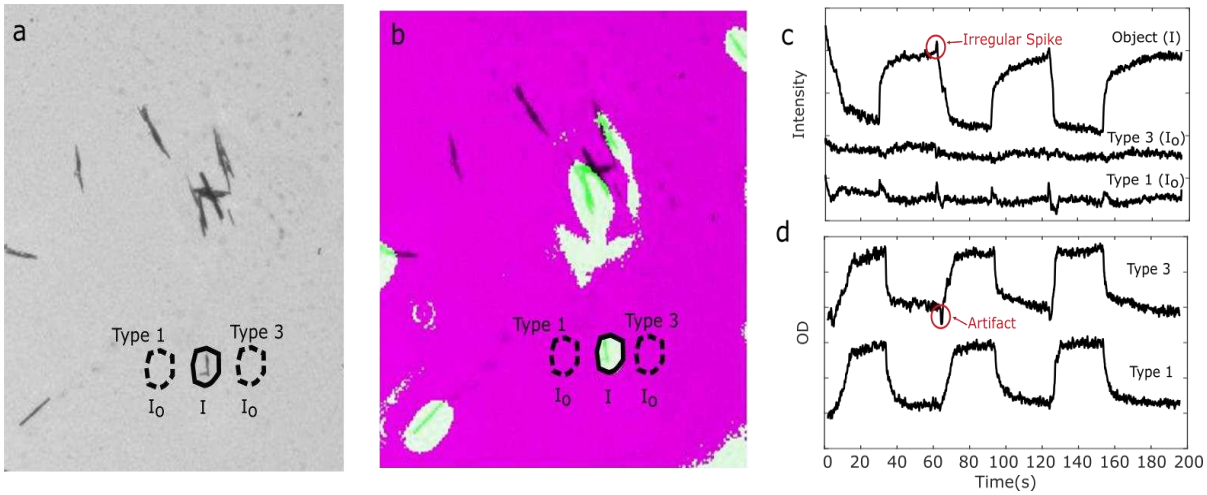

Figure 7. a) TEM image of WO_3 nanoparticles on a TEM grid. Object of interest is circled in solid black, with corresponding background masks (dashed black) drawn to the left and right. b) Overlay image of TEM transformed and optical binary images. The same masks drawn in panel a) are placed at the same coordinates in panel b. c) Three raw intensity trajectories corresponding to the three masks drawn on the images in panel a & b. d) Two optical density trajectories are shown corresponding to the two background masks shown in panel a & b. The Type 3 background mask results in an artifact in the OD trajectory, circled in red.

To further quantify how the electrochemically induced mechanical properties of the carbon film impacts the electro-optical response of WO_3 nanoparticles, we collect 89 nanoparticle background trajectories and sort the background behaviors into the 4 types. To sort the background behaviors, two to three prospective background masks are drawn around the object of interest as shown in Figure 7a & b. The integrated pixel intensity of the three masks as a function of time is shown in Figure 7c. The prospective background masks are used to compute what the optical density trajectory is with each background mask, as shown in Figure 7d. Because the optical trajectory of this material is well understood, we note an irregular spike, circled in red, in intensity in the object intensity trajectory that is not attributed to particle activity (Figure 7c).[1] We conclude that this irregular spike is a manifestation of the carbon film optical activity convoluted in the

particle or object intensity trajectory. To properly correct for the carbon film optical activity, we select a background mask which eliminates this irregularity or artifact. To do so in this example, we select the Type 1 background trace, which removes the artifact in Figure 7d, therefore correcting for the optical activity of the carbon film and assigning this particle to a Type 1 background. We perform this procedure for all 89 objects to determine what type of background a particle is on.

Furthermore, we determine how active a particle is by calculating the maximum optical density (max OD). To calculate the max OD, we average the last 5 OD data points of the 3 coloring potential pulses. This value represents the highest OD value a particle achieves when it is colored. When a particle is sorted to a background type, the max OD is also calculated and plotted on the x axis, producing Figure 8. Due to the low number of particles (3) found on a Type 4 background, we exclude those particles from this quantitative analysis. We then determine a threshold of optical activity to quantify which particles are active vs inactive. This activity threshold (0.0025) is calculated by determining the maximum OD change of a Type 3 background area. This threshold reveals what percentage of particles on each background type are active or inactive. Through this quantitative analysis we determine that particles on a Type 3 background are less likely to be active (32%) compared to particles on Type 1 or Type 2 background (58% and 63% respectively). The optical activity of Type 1 and Type 2 background indicates that the carbon film is reacting to the applied electric field. We assume that particles that are lying on this area of carbon film are exposed to this applied electric field and electrochromic behavior of these particles is more likely. Conversely, the lack of optical activity exhibited by Type 3 indicates that the applied electric field is less in that area of the carbon film thus particles on that background are less likely to exhibit electrochromic behavior. This indicates that the local electrical conductivity of the carbon film is

dynamic. Of the particles analyzed, 58 of 89 are on a Type 3 background implying that the majority of the carbon film is of Type 3 nature and suggests that the lowered optical activity of particles on a TEM substrate is due to local lowered electric field on the carbon film.

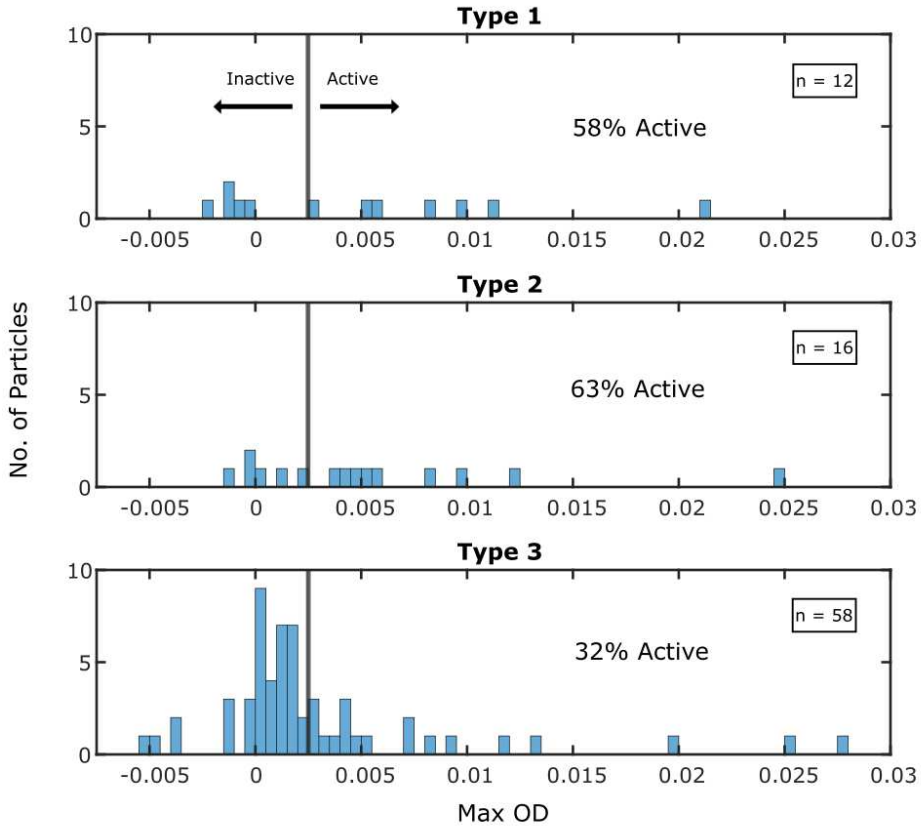

Figure 8. Nanoparticle objects were sorted by type of background a particle laid on and max OD. A maximum OD threshold was established to distinguish active and inactive particles. The percent of active particles of a certain type are cited to the right of the corresponding histograms.

Single Particle Correlated Electro-optical TEM Analysis

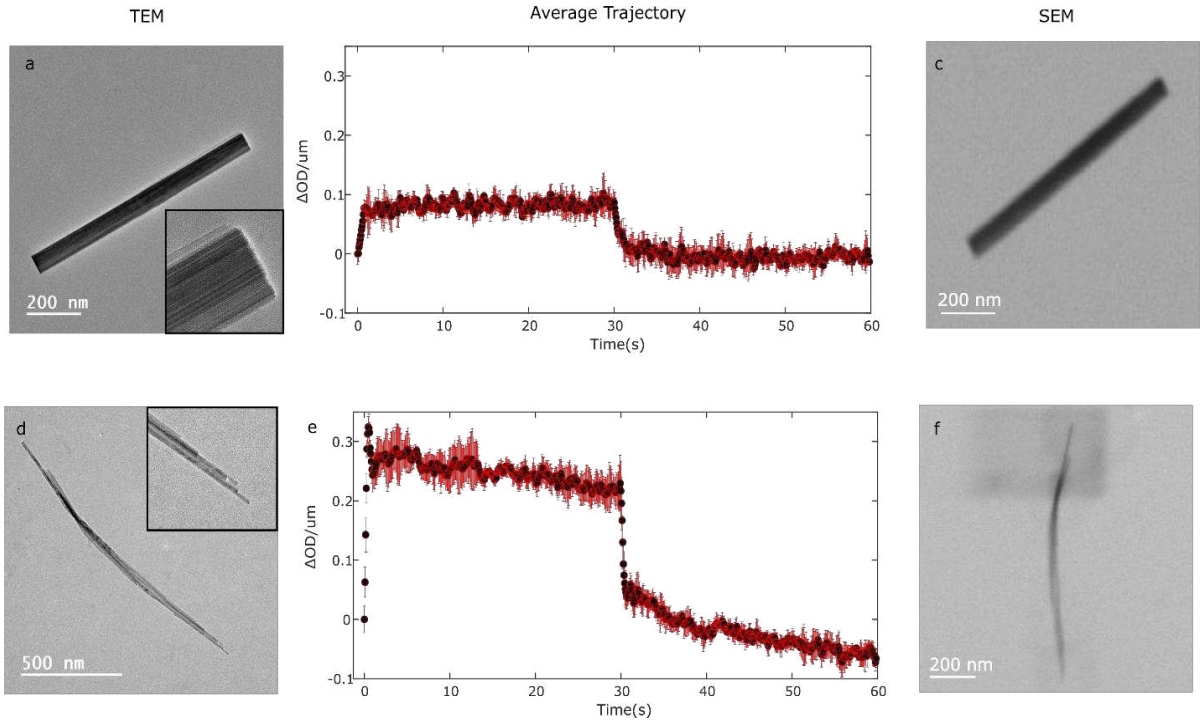

Figure 9. a & d) TEM micrographs of WO_3 nanoparticles. The inset in d) is a zoomed and cropped image of the right end of the particle in d) illustrating the presence of step edges. b & e) Trajectories of particles shown in a & d) respectively. These trajectories are produced by taking the OD(t) of 3 coloring pulses and averaging the OD values (shown in black) and the standard deviation (shown in red). c & f) SEM micrographs of the same nanoparticles shown in a & d) respectively.

Using the methods and analysis outlined in Figure 2, Figure *3*, & 4 and considering the anomalous behavior of the background, we then purse examination of single particles. Of the 89 particles analyzed, two single particles were spatially resolved and optically active. Figure 9a & d are TEM micrographs of the single particles of interest. We calculate the average OD(t) trajectory of these two particles over the course of 3 cathodic and anodic potential pulses and compare the optical behavior of these two particles after correcting for thickness, according to Beer-Lambert Law[39], shown in Figure 9b & e. Scanning electron microscope (SEM) images are shown in Figure 9c & f to compare the enhanced resolution TEM provides, revealing step edges that would not be resolved using SEM alone. The goal of this study is to better understand how finite structural characteristics of a single particle can lead to differences in optical behavior. We analyze common

optical parameters presented in smart windows-related research such as maximum optical density (max OD), and the time it takes to achieve 90% of the maximum optical density(t_{90}). The max OD is calculated by taking the mean of the last 5 data points of the average trajectory and t_{90} is found by determining the time at which OD reaches 90% of the max OD value. We observe the particle in Figure 9d to reach a max OD of 0.2192 while the max OD reached by the particle in Figure 9a is 0.0826. When comparing these two particles, the particle in Figure 9d absorbs nearly 3 times more 940 nm light than the particle in Figure 9a. For these two particles the $t_{90} = 0.15$ seconds for the particle in Figure 9d and $t_{90} = 0.745$ seconds for the particle in Figure 9a. In summary, the particle in Figure 9d turns color faster and darker.

To understand why this particle has a higher and faster coloration efficiency we consider how Li^+ ions insert into the crystal structure of *h*-WO_3. Hibino *et al* determined that hexagonal window tunnels are present along the c axis of *h*-WO_3 and enable ion transport through the bulk of a nanoparticle.[44] We observe the presence of a particle dependent surface step structure characteristic on the particle in Figure 9d, that is not present in Figure 9a. A cartoon representation of this step edge feature is shown in Figure 10. These step edges towards the end of the nanoparticle expose a higher surface area of hexagonal windows at the terminal ends of a single nanoparticle.

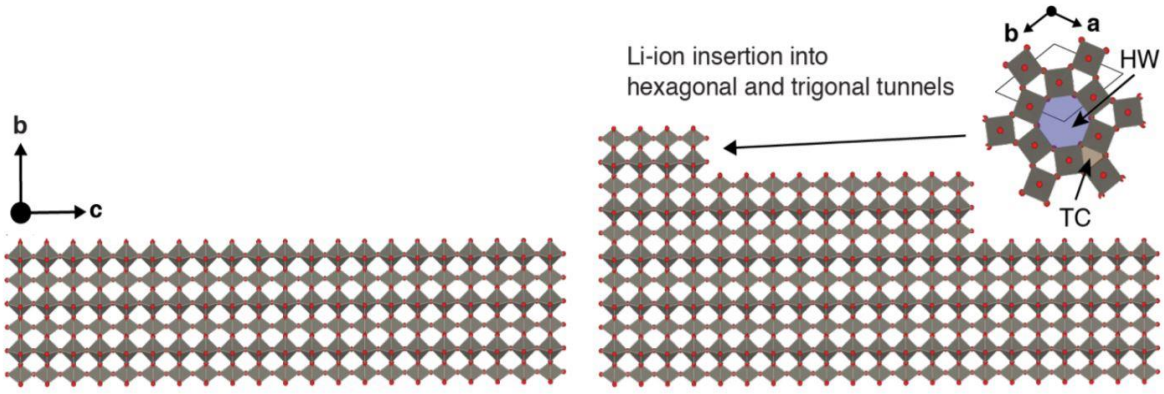

Figure 10. Two illustrations of the crystal structure of *h*-WO_3. The left illustration represents a particle with no step-edges along the length. The right illustration represents a particle with step-edges along the length of the rod.

Further analysis of the crystal structure of this material reveals that these hexagonal windows are present along the length of the particle and act as tunnels along the c-axis of this material. These step-edges would increase Li^+ ion access into the material through these hexagonal tunnels. (Figure 10) Therefore, these step edges may provide more reaction pathways in which ions can insert into the material, leading to a faster color change as well as a deeper color change. We attribute this step edge structural feature to the enhanced optical behavior the nanoparticle. Only with this method can we use TEM to characterize step-edges on a single nanoparticle while also collecting rich electrochemical information of the same single particle via it's electrochromic behavior. There have been studies analyzing the electrochemical behavior of single nanoparticles on a TEM grid performed previously. Abruña and co-authors developed an electrochemical cell utilizing a TEM grid working electrode, in order to perform electron tomography of Pt−Co nanocatalyst particles before and after electrochemical aging[46]. However, with this method, they lack the link to single particle-level electrochemical data with high resolution structural behavior. In order to enhance the methodology introduced by this study, it is worth implementing an aspect of collecting electrochemical data of the single particles to be structurally characterized. This study provides one method to collect rich electrochemical and structural information to better establish the structure-activity relationship present among heterogenous single nanoparticles.

Conclusions

This work outlines an electro-optical bright field transmission microscopy experiment that permits correlated *ex-situ* TEM imaging. Using this methodology grants TEM resolution of single particles and the ability measure the optical activity of those same particles. Image processing reveals heterogenous optical activity of *h*-WO_3 nanoparticles on a TEM grid substrate. Due to the heterogeneous optical activity of the carbon film, determination of the incident light in this system is a challenge that must be considered when performing electro-optical measurements on a TEM grid with carbon support. Measuring the optical activity of WO_3 on a carbon support film is still possible, considering this challenge, and quantitative measurements are taken of two nanoparticles. This study indicates that the presence of a step edge gradient leads to more access to ion insertion pathways by opening more hexagonal window channels along the c-axis of this material. This expanded access to hexagonal window channels leads to faster and deeper coloration of a *h*-WO_3 single nanorods.

Outlook

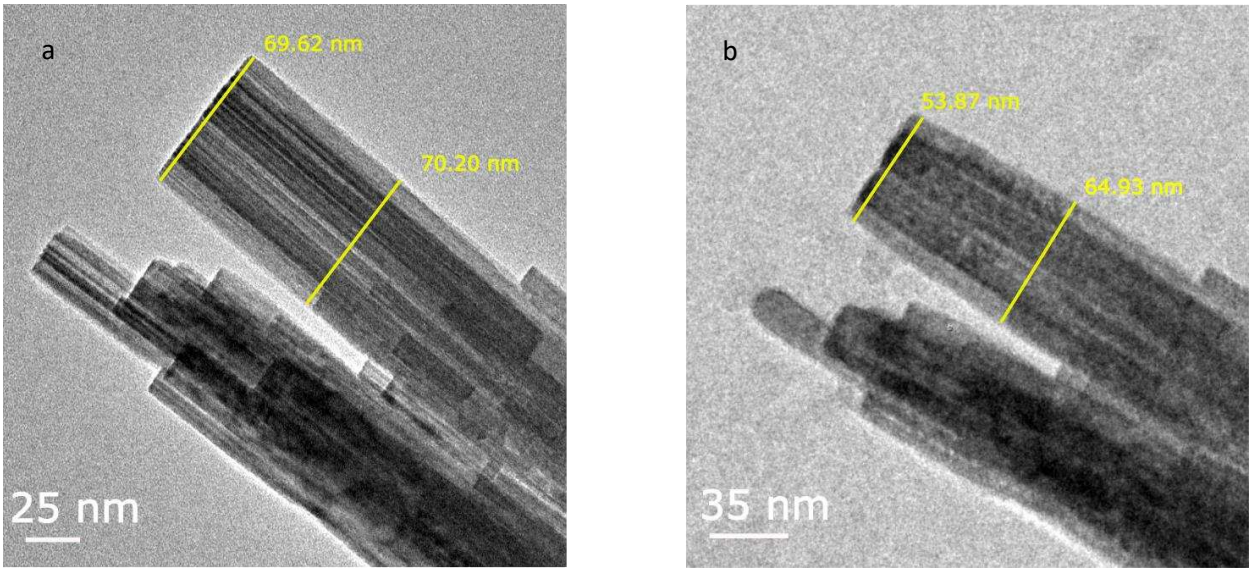

Figure 11. a) TEM micrograph of pristine WO3 nanoparticles with width measurements along the rod. b) TEM micrograph of the same particles shown in a) after lithiation for 3 hrs.

The method presented in this body of work can contribute to the better understanding of the fundamental dynamics of structural changes that occur upon ion insertion into a material. Using TEM we can measure how WO_3 rods structurally change upon lithiation with nanometer resolution. Figure 11 shows a cluster of nanoparticles in the as deposited pristine condition (Figure 11a) and the same nanoparticles after applying a cathodic, coloring, potential for three hours(Figure 11b). Using this method, it is possible to resolve nanometer scale structural changes between the two images. The ends of the particle curved and contracted from 69.92 nm to 53.87 nm after lithiation, a contraction of 23%. Further along the rod contraction continues to occur, though less so than at the ends, with contraction of 7%. Though not pictured in Figure 11, the length of the rod contracted by 6.7%. These results indicate that upon lithiation, the entire nanoparticle contracts. However, it is also evident that the ends of the nanoparticle contract more so compared to the bulk of the nanoparticle. This observation implies that lithiation of this material is non-uniform along

the length of the nanoparticle. Only with this method it is possible to take measurements with selected area electron diffraction (SAED) along the length of a nanoparticle. By doing so we can further investigate the local lattice parameter changes of these rods along the c axis.

References

(1) Evans, R. C.; Ellingworth, A.; Cashen, C. J.; Weinberger, C. R.; Sambur, J. B. Influence of Single-Nanoparticle Electrochromic Dynamics on the Durability and Speed of Smart Windows. *Proc. Natl. Acad. Sci. U. S. A.* **2019**, 201822007.

(2) Sbar, N. L.; Podbelski, L.; Yang, H. M.; Pease, B. Electrochromic Dynamic Windows for Office Buildings. *Int. J. Sustain. Built Environ.* **2012**, *1* (1), 125–139.

(3) DeForest, N.; Shehabi, A.; O'Donnell, J.; Garcia, G.; Greenblatt, J.; Lee, E. S.; Selkowitz, S.; Milliron, D. J. United States Energy and CO2 Savings Potential from Deployment of Near-Infrared Electrochromic Window Glazings. *Build. Environ.* **2015**, *89*, 107–117.

(4) Granqvist, C. G.; Arvizu, M. A.; Bayrak Pehlivan, İ.; Qu, H.-Y.; Wen, R.-T.; Niklasson, G. A. Electrochromic Materials and Devices for Energy Efficiency and Human Comfort in Buildings: A Critical Review. *Electrochim. Acta* **2018**, *259*, 1170–1182.

(5) Cai, G.; Wang, J.; Lee, P. S. Next-Generation Multifunctional Electrochromic Devices. *Acc. Chem. Res.* **2016**, *49* (8), 1469–1476.

(6) Runnerstrom, E. L.; Llordés, A.; Lounis, S. D.; Milliron, D. J. Nanostructured Electrochromic Smart Windows: Traditional Materials and NIR-Selective Plasmonic Nanocrystals. *Chem. Commun.* **2014**, *50* (73), 10555–10572.

(7) Masashi Okubo, †,⊥; Eiji Hosono, †; Jedeok Kim, ‡; Masaya Enomoto, §; Norimichi Kojima, §; Tetsuichi Kudo, †; Haoshen Zhou, † and; Itaru Honma*, †. Nanosize Effect on High-Rate Li-Ion Intercalation in LiCoO2 Electrode. **2007**.

(8) Qi, K.; Wei, J.; Sun, M.; Huang, Q.; Li, X.; Xu, Z.; Wang, W.; Bai, X. Real-Time Observation of Deep Lithiation of Tungsten Oxide Nanowires by In Situ Electron Microscopy. *Angew. Chemie Int. Ed.* **2015**, *54* (50), 15222–15225.

(9) Cong, S.; Tian, Y.; Li, Q.; Zhao, Z.; Geng, F. Single-Crystalline Tungsten Oxide Quantum Dots for Fast Pseudocapacitor and Electrochromic Applications. *Adv. Mater.* **2014**, *26* (25), 4260–4267.

(10) Giannuzzi, R.; Scarfiello, R.; Sibillano, T.; Nobile, C.; Grillo, V.; Giannini, C.; Cozzoli, P. D.; Manca, M. From Capacitance-Controlled to Diffusion-Controlled Electrochromism in One-Dimensional Shape-Tailored Tungsten Oxide Nanocrystals. *Nano Energy* **2017**, *41*, 634–645.

(11) Wang, J.; Khoo, E.; Lee, P. S.; Ma, J. Synthesis, Assembly, and Electrochromic Properties of Uniform Crystalline WO 3 Nanorods. *J. Phys. Chem. C* **2008**, *112* (37), 14306–14312.

(12) Liu, R.; Zhang, H. Y.; Ji, Z. X.; Rallo, R.; Xia, T.; Chang, C. H.; Nel, A.; Cohen, Y. Development of Structure–Activity Relationship for Metal Oxide Nanoparticles. *Nanoscale* **2013**, *5* (12), 5644.

(13) Bresee, J.; Bond, C. M.; Worthington, R. J.; Smith, C. A.; Gifford, J. C.; Simpson, C. A.; Carter, C. J.; Wang, G.; Hartman, J.; Osbaugh, N. A.; et al. Nanoscale Structure–Activity Relationships, Mode of Action, and Biocompatibility of Gold Nanoparticle Antibiotics. *J. Am. Chem. Soc.* **2014**, *136* (14), 5295–5300.

(14) Ebejer, N.; Schnippering, M.; Colburn, A. W.; Edwards, M. A.; Unwin, P. R. Localized High Resolution Electrochemistry and Multifunctional Imaging: Scanning Electrochemical Cell Microscopy. *Anal. Chem.* **2010**, *82* (22), 9141–9145.

(15) Ishiguro, N.; Kityakarn, S.; Sekizawa, O.; Uruga, T.; Sasabe, T.; Nagasawa, K.; Yokoyama, T.; Tada, M. Rate Enhancements in Structural Transformations of Pt–Co and Pt–Ni Bimetallic Cathode Catalysts in Polymer Electrolyte Fuel Cells Studied by in Situ Time-

Resolved X-Ray Absorption Fine Structure. *J. Phys. Chem. C* **2014**, *118* (29), 15874–15883.
(16) Jiang, D.; Jiang, Y.; Li, Z.; Liu, T.; Wo, X.; Fang, Y.; Tao, N.; Wang, W.; Chen, H.-Y. Optical Imaging of Phase Transition and Li-Ion Diffusion Kinetics of Single $LiCoO_2$ Nanoparticles During Electrochemical Cycling. *J. Am. Chem. Soc.* **2017**, *139* (1), 186–192.
(17) Wang, F.; Yu, H.-C.; Chen, M.-H.; Wu, L.; Pereira, N.; Thornton, K.; Van der Ven, A.; Zhu, Y.; Amatucci, G. G.; Graetz, J. Tracking Lithium Transport and Electrochemical Reactions in Nanoparticles. *Nat. Commun.* **2012**, *3* (1), 1201.
(18) Wang, C. M.; Xu, W.; Liu, J.; Choi, D. W.; Arey, B.; Saraf, L. V; Zhang, J. G.; Yang, Z. G.; Thevuthasan, S.; Baer, D. R.; et al. In Situ Transmission Electron Microscopy and Spectroscopy Studies of Interfaces in Li Ion Batteries : Challenges and Opportunities. **2018**, No. 8.
(19) Nachimuthu, P.; Matsuo, S.; Farangis, B.; Lindle, D. W.; Wakita, H.; Perera, R. C. C. Electronic and Structural Properties of 'Smart Windows' and Liquids Using in-Situ X-Ray Absorption Spectroscopy. *J. Alloys Compd.* **2004**, *362* (1–2), 124–132.
(20) Balaji, S.; Djaoued, Y.; Albert, A.-S.; Ferguson, R. Z.; Brüning, R. Hexagonal Tungsten Oxide Based Electrochromic Devices: Spectroscopic Evidence for the Li Ion Occupancy of Four-Coordinated Square Windows. *Chem. Mater.* **2009**, *21*, 1381–1389.
(21) Wilson, A. J.; Willets, K. A. Visualizing Site-Specific Redox Potentials on the Surface of Plasmonic Nanoparticle Aggregates with Superlocalization SERS Microscopy. *Nano Lett.* **2014**, *14* (2), 939–945.
(22) Larsson, A.-L.; Sernelius, B. E.; Niklasson, G. A. Optical Absorption of Li-Intercalated Polycrystalline Tungsten Oxide Films: Comparison to Large Polaron Theory. **2003**.
(23) Liu, X. H.; Zhang, L. Q.; Zhong, L.; Liu, Y.; Zheng, H.; Wang, J. W.; Cho, J.-H.; Dayeh, S. A.; Picraux, S. T.; Sullivan, J. P.; et al. Ultrafast Electrochemical Lithiation of Individual Si Nanowire Anodes. *Nano Lett.* **2011**, *11* (6), 2251–2258.
(24) Gu, M.; Parent, L. R.; Mehdi, B. L.; Unocic, R. R.; McDowell, M. T.; Sacci, R. L.; Xu, W.; Connell, J. G.; Xu, P.; Abellan, P.; et al. Demonstration of an Electrochemical Liquid Cell for Operando Transmission Electron Microscopy Observation of the Lithiation/Delithiation Behavior of Si Nanowire Battery Anodes. *Nano Lett.* **2013**, *13* (12), 6106–6112.
(25) Xie, Z.-H.; Jiang, Z.; Zhang, X. Review—Promises and Challenges of In Situ Transmission Electron Microscopy Electrochemical Techniques in the Studies of Lithium Ion Batteries. *J. Electrochem. Soc.* **2017**, *164* (9), A2110–A2123.
(26) Wu, Y.; Liu, N. Visualizing Battery Reactions and Processes by Using In Situ and In Operando Microscopies. *Chem* **2018**, *4* (3), 438–465.
(27) Zhang, W.; Yu, H.-C.; Wu, L.; Liu, H.; Abdellahi, ‡ Aziz; Qiu, B.; Bai, J.; Orvananos, B.; Strobridge, F. C.; Zhou, X.; et al. *Localized Concentration Reversal of Lithium during Intercalation into Nanoparticles*; 2018.
(28) Qi, K.; Li, X.; Sun, M.; Huang, Q.; Wei, J.; Xu, Z.; Wang, W.; Bai, X.; Wang, E. *In-Situ* Transmission Electron Microscopy Imaging of Formation and Evolution of $Li_x WO_3$ during Lithiation of WO_3 Nanowires. *Appl. Phys. Lett.* **2016**, *108* (23), 233103.
(29) Momotenko, D.; Byers, J. C.; McKelvey, K.; Kang, M.; Unwin, P. R. High-Speed Electrochemical Imaging. *ACS Nano* **2015**, *9* (9), 8942–8952.
(30) Tao, B.; Yule, L. C.; Daviddi, E.; Bentley, C. L.; Unwin, P. R. Correlative Electrochemical Microscopy of Li-Ion (De)Intercalation at a Series of Individual $LiMn_2O_4$ Particles. *Angew. Chemie* **2019**, *131* (14), 4654–4659.

(31) Granqvist, C. . Electrochromic Tungsten Oxide Films: Review of Progress 1993–1998. *Sol. Energy Mater. Sol. Cells* **2000**, *60* (3), 201–262.
(32) Deb, S. K. Opportunities and Challenges in Science and Technology of WO3 for Electrochromic and Related Applications. *Sol. Energy Mater. Sol. Cells* **2008**, *92* (2), 245–258.
(33) Georg, A.; Georg, A.; Graf, W.; Wittwer, V. Switchable Windows with Tungsten Oxide. *Vacuum* **2008**, *82* (7), 730–735.
(34) Monk, P. M. S.; Monk, P. M. S. *Charge Movement through Electrochromic Thin- Film Tungsten Trioxide Charge Movement through Electrochromic Thin-Film Tungsten Trioxide*; 2017; Vol. 8436.
(35) Mortimer, R. J. Electrochromic Materials. *Annu. Rev. Mater. Res.* **2011**, *41* (1), 241–268.
(36) Slade, R. C. T.; West, B. C.; Hall, G. P. Chemical and Electrochemical Mixed Alkali Metal Insertion Chemistry of the Hexagonal Tungsten Trioxide Framework. *Solid State Ionics* **1989**, *32–33*, 154–161.
(37) Lee, Y.; Lee, T.; Jang, W.; Soon, A. Unraveling the Intercalation Chemistry of Hexagonal Tungsten Bronze and Its Optical Responses.
(38) Llordés, A.; Garcia, G.; Gazquez, J.; Milliron, D. J. Tunable Near-Infrared and Visible-Light Transmittance in Nanocrystal-in-Glass Composites. *Nature* **2013**, *500* (7462), 323–326.
(39) Scarminio, J.; Urbano, A.; Gardes, B. The Beer-Lambert Law for Electrochromic Tungsten Oxide Thin Films. *Mater. Chem. Phys.* **1999**, *61* (2), 143–146.
(40) Fosdick, S. E.; Anderson, M. J.; Nettleton, E. G.; Crooks, R. M. Correlated Electrochemical and Optical Tracking of Discrete Collision Events. *J. Am. Chem. Soc.* **2013**, *135* (16), 5994–5997.
(41) Li, K.; Wang, K.; Qin, W.; Deng, S.; Li, D.; Shi, J.; Huang, Q.; Fan, C. DNA-Directed Assembly of Gold Nanohalo for Quantitative Plasmonic Imaging of Single-Particle Catalysis. *J. Am. Chem. Soc.* **2015**, *137* (13), 4292–4295.
(42) Patel, A. N.; Martinez-Marrades, A.; Brasiliense, V.; Koshelev, D.; Besbes, M.; Kuszelewicz, R.; Combellas, C.; Tessier, G.; Kanoufi, F. Deciphering the Elementary Steps of Transport-Reaction Processes at Individual Ag Nanoparticles by 3D Superlocalization Microscopy. *Nano Lett.* **2015**, *15* (10), 6454–6463.
(43) Brasiliense, V.; Clausmeyer, J.; Dauphin, A. L.; Noël, J.-M.; Berto, P.; Tessier, G.; Schuhmann, W.; Kanoufi, F. Opto-Electrochemical In Situ Monitoring of the Cathodic Formation of Single Cobalt Nanoparticles. *Angew. Chemie Int. Ed.* **2017**, *56* (35), 10598–10601.
(44) Hibino, M.; Han, W.; Kudo, T. Electrochemical Lithium Intercalation into a Hexagonal WO3 Framework and Its Structural Change. *Solid State Ionics* **2000**, *135* (1–4), 61–69.
(45) Wen, Y.; Chen, X.; Lu, X.; Gu, L. Interface Charges Boosted Ultrafast Lithiation in Li4Ti5O12 Revealed by In-Situ Electron Holography. *J. Energy Chem.* **2018**, *27* (5), 1397–1401.
(46) Yu, Y.; Xin, H. L.; Hovden, R.; Wang, D.; Rus, E. D.; Mundy, J. A.; Muller, D. A.; Abruña, H. D. Three-Dimensional Tracking and Visualization of Hundreds of Pt-Co Fuel Cell Nanocatalysts during Electrochemical Aging. *Nano Lett.* **2012**, *12* (9), 4417–4423.